



CrossMark  
click for updates

Cite this: *RSC Adv.*, 2016, 6, 110758

# Ultrafine N-doped carbon nanoparticles with controllable size to enhance electrocatalytic activity for oxygen reduction reaction†

Wenxi Wang,‡ Yang Shi,‡ Minchan Li, Zhenyu Wang, Shaofei Wu, Fucong Lyu, Chaoqun Shang and Zhouguang Lu\*

There are several drawbacks to the current oxygen reduction reaction (ORR) involving the kinetically sluggish process and expensive catalysts which impede the mass production of noble-metal materials for application in clean and efficient energy conversion devices. Herein, a type of ultrafine carbon nanoparticle with high nitrogen doping concentration can be simply prepared from a conveniently available precursor through a green and cost-effective hydrothermal process. With the aid of water, not only is the product's specific surface area enlarged, but the pore structure is also enriched, and there is improvement in the degree of graphitization and nitrogen-doped content. Meanwhile, the size of the carbon particle can be readily tuned to a nanoscale by changing the duration of the hydrothermal reaction. Interestingly, electrocatalytic activity is dramatically enhanced with the transformation of the carbon size and nitrogen structure. The characterization reveals that we have achieved a highly satisfactory electrocatalytic activity for ORR, a relatively positive onset potential of  $-0.02$  V (vs. Hg/HgO) in alkaline media and  $0.55$  V (vs. Ag/AgCl) in acidic media, a higher diffusion-limiting current density than that of Pt/C, as well as outstanding stability and superior tolerance durability to methanol. Both the simplicity of the operation and the employed biomass precursor exactly meet the criteria for significant cost-saving, easy scale-up and eco-friendly demands for energy storage.

Received 4th September 2016  
Accepted 13th November 2016

DOI: 10.1039/c6ra22145a

[www.rsc.org/advances](http://www.rsc.org/advances)

## 1 Introduction

The increasing global energy crisis and environmental contamination have stimulated worldwide efforts to rationally explore alternative clean and sustainable energy generation.<sup>1–3</sup> In particular, it is highly anticipated that fuel cells and metal–air batteries will be adopted in the automotive field in the future.<sup>4,5</sup> Nevertheless, outside the confinement of the sluggish kinetics of ORR at the cathode, sufficient high-efficiency electrocatalysts are generally desired for practical applications. State of the art electrocatalysts used in the ORR predominantly rely on the best known platinum or its alloys,<sup>6–9</sup> although the high cost and declining activity of these noble metal-bases have severely obstructed their widespread commercialization.<sup>10–14</sup> In this regard, researchers have their hearts set on extensively developing highly active and cost-effective non-precious metal catalysts<sup>15–18</sup> or metal-free heteroatom-enriched (*e.g.* N, B, S and P) carbonaceous materials<sup>19–21</sup> for the four-electron ( $4e^-$ ) ORR.

Recent progress has resulted in the incorporation of heteroatoms (N, P and B) into a  $sp^2$ -hybridized carbon framework, giving rise to enhanced electrocatalytic activities and reaction kinetics as a result of the changes in the charge and spin densities of the carbon lattice, which originates from the difference in electronegativity between carbon atoms and heteroatoms.<sup>19,22–25</sup> In the past, the most frequently employed approaches to multiple-doping carbon have been high temperature post-treatment, the electrochemical method, liquid phase polymerization and plasma treatment or chemical vapour deposition.<sup>19,26–36</sup> These methods are generally deficient and involve tedious and complex experimental procedures or harsh reaction conditions due to the inclusion of various synthetic chemicals. In the current case, it is expected that heteroatom doping will be realized by simple and eco-friendly methods for fabrication of affordable carbonaceous material and ultimately be employed as a substitute for Pt-based ORR electrocatalysis. Moreover, it is widely accepted that low catalytic sites offer the nonuniform and insufficient exposure of the active catalytic sites of pyrolytic products,<sup>37–39</sup> which is influenced, to a large extent, by the size, shape and nanoscale porosity of the electrocatalyst. As catalytic character alters different with carbonaceous precursors, a large quantity of precursors have been investigated over past years. To date, the precursor development of doped carbon material has moved

Department of Material Science and Engineering, South University of Science and Technology of China, Shenzhen, Guangdong 518055, China. E-mail: luzg@sustc.edu.cn

† Electronic supplementary information (ESI) available. See DOI: 10.1039/c6ra22145a

‡ These authors contribute equally to this job.

from expensive, hazardous inorganic and organic chemicals to sustainable biomass,<sup>40–42</sup> such as edible biomass and organic-rich wastes.

At this juncture, it is therefore meaningful to directly design a type of well-structured porous and heteroatom doping carbon material from conveniently available biomass without using any synthetic chemicals, which also simplifies the procedure and decreases expense. The spindle-shaped *Sterculia scaphigera*, commonly found as an affordable herbal remedy in Indonesian and Chinese medicine, primarily consists of bassorin, galactose and pentaglucoase. Based on the previous work,<sup>43</sup> the natural *Sterculia scaphigera* expands significantly in volume when immersed in hot water, and hence an abundant pore structure develops as it is moved in and out of water. Moreover the morphology has a significant variation through hydrothermal treatment, tending to produce nanospheres with a diameter of several nanometers. To the best of our knowledge, this is the first recorded instance that microporous nanosphere-shaped carbon has been prepared from natural biomass *Sterculia scaphigera*, which displays highly efficient and selective catalytic activity in ORR.

## 2 Experimental section

### 2.1 Preparation of microporous carbon nanoparticles (MCN)

For the synthesis of MCN, 50 g of thoroughly dried *Sterculia scaphigera* (Fig. 1a) was first immersed into hot water of approximately at 80 °C for 2 h. After immersion, the volume of dried *Sterculia scaphigera* will swell significantly, as shown in Fig. 1b. The transparent colloform analogs were selected as a hydrothermal precursor, and subsequently treated in a Teflon lined autoclave at 180 °C for several hours. To identify the effect of hydrothermal time on the oxygen reduction reaction activity, the precursor was treated for 6, 12 and 18 h, respectively. Subsequently, the products were collected through centrifugation at 9000 rpm for 5 min several times, and then dried in a freezer dryer for overnight. All precursors were then carbonized as the following process. The temperature was increased from ambient temperature to 250 °C at a speed of 1 °C min<sup>-1</sup>,

further kept for 2 h in Ar atmosphere. Thereafter, the temperature sequentially increased to 800, 900 and 1000 °C at a heating rate of 5 °C min<sup>-1</sup>, and remained final temperature for 1.5 h. For simplicity, the carbon specimens were denoted as MCN-800, MCN-900, MCN-1000. Separately, the carbon material was obtained from direct carbonization of raw *Sterculia scaphigera* without water assistance and hydrothermal process at 900 °C, which labeled as R-900. Finally, another sample only absorbed abundant water was treated by freeze drying and carbonized at 900 °C, which is designated as A-900.

### 2.2 Physical characterizations

High-resolution TEM (JEOL, JEM-2010F at 200 kV) and field emission SEM (FESEM, JEOL 7001F) were performed to characterize the size and morphologies of the prepared materials. The degree of graphitization these samples was also detected by Raman spectroscopy using Jobin-Yvon T6400 confocal Raman spectrometer with 532 nm diode laser excitation on 1800-line grating. Nitrogen adsorption/desorption isotherms were measured on a Micromeritics, ASAP2020 gas sorption analyzer at 77 K. All samples were firstly degassed at 200 °C on a vacuum line following a standard protocol before measurement. The specific surface area was determined from N<sub>2</sub> adsorption isotherm by applying Brunauer–Emmett–Teller (BET) theory and the pore size distributions were obtained from the adsorption branch by means of Barrette–Joynere–Halenda (BJH). The total pore volumes were determined from the amount adsorbed at high relative pressure of 0.99. X-ray photoelectron spectroscopy (XPS) was investigated using a VG scientific ESCALAB 220iXL spectrometer with an Al K $\alpha$  ( $h\nu = 1486.69$  eV) X-ray source. All binding energies were carefully aligned by reference to the C 1s peak (284.6 eV) arising from surface hydrocarbons or possible adventitious hydrocarbon.

### 2.3 Electrochemical measurements

**2.3.1 Rotating disk electrode (RDE) measurement.** The electrochemical experiments were carried out in a conventional three-electrode cell using a Bio-Logic VMP3 workstation controlled at ambient temperature. Platinum, Hg/HgO and Ag/AgCl were used as the counter and reference electrodes, respectively. A glass carbon (GC) disk with a diameter of 5.0 mm served as the substrate for the working electrode. To coat the working electrode with that catalyst, typically, 2 mg of each sample was ultrasonically dispersed in the 1 ml water/isopropanol (v/v = 1 : 3) mix solvent for 1 h. Then a GC electrode was covered with 5  $\mu$ l of the catalyst ink, which was further adhered using 5  $\mu$ l 0.05 wt% Nafion solutions. The electrolyte was saturated with pure oxygen by bubbling O<sub>2</sub> in 0.1 M KOH and 0.1 M HClO<sub>4</sub> solution before each electrochemical experiment. The cyclic voltammetry (CV) and oxygen reduction tests were completed by rotating the electrode in the range of 400 rpm to 2025 rpm at a scanning rate of 10 mV s<sup>-1</sup>. The CV measurements were also performed in Ar flow for control experiments. The stability of the catalyst possessing outstanding ORR was evaluated by 2000 cycles at a sweep rate of 10 mV s<sup>-1</sup>. Koutecky–Levich plots were analyzed at different

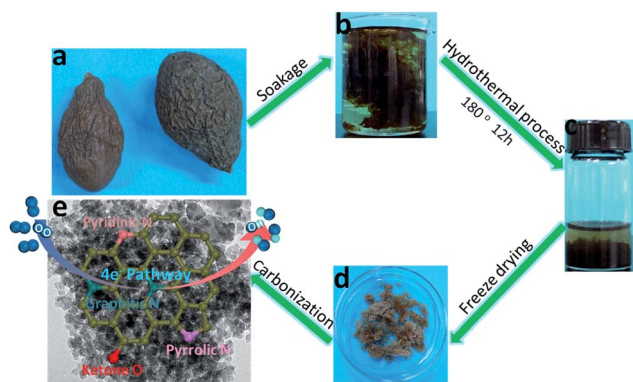


Fig. 1 Schematic process for preparation of the carbon nanoparticles. Images of the biomass (a) *Sterculia scaphigera*; and (b) biomass having absorbed water; (c) sample for hydrothermal treatment and (d) freeze drying; (e) carbonaceous material.

electrode potentials. The slopes of their best linear fit lines were used to calculate the number of electrons transferred ( $n$ ) on the basis of the Koutecky–Levich equation:<sup>44,45</sup>

$$\frac{1}{J} = \frac{1}{J_L} + \frac{1}{J_k} = \frac{1}{B\omega^{1/2}} + \frac{1}{J_k}$$

$$B = 0.62nFC_o(D_o)^{2/3}v^{-1/6}$$

where  $J$  is the measured current,  $J_k$  is the kinetic-limiting current and  $\omega$  is the electrode rotation angular velocity.  $n$  is the transferred electron number,  $F$  is the Faraday constant,  $C_o$  is the bulk concentration of  $O_2$ ,  $D_o$  is the diffusivity of  $O_2$  molecule in the electrolyte, and  $\nu$  is the kinematic viscosity of the electrolyte. For the Tafel plot, the kinetic current was obtained from the mass-transport correction of RDE by:

$$J_k = \frac{J \times J_L}{J_L - J}$$

### 2.3.2 Rotating ring-disk electrode (RRDE) measurement.

Catalyst and electrodes were prepared by the same method as above. The ring current ( $I_r$ ) was measured with a Pt ring electrode in the alkaline and acidic solution. The four-electron selectivity of the catalyst was evaluated based on the  $H_2O_2$  yield. The  $H_2O_2$  yield and the electron transfer number ( $n$ ) were determined by the following equations:

$$\% HO_2^- = 200 \times \frac{I_r/N}{I_d + I_r/N}$$

$$n = 4 \times \frac{I_d}{I_d + I_r/N}$$

where  $I_d$  is the disk current,  $I_r$  is the ring current, and  $N$  is current collection efficiency of the Pt ring.  $N$  is 0.32 from the reduction of  $K_3Fe[CN]_6$ .<sup>46</sup>

## 3 Results and discussion

### 3.1 Micromorphology and composition

Fig. 2a and S1† present the SEM morphology of the three specimens as prepared before carbonization. Obviously, the SEM image of Fig. S1d† shows distinct micro-appearance differences with raw *Sterculia scaphigera* (Fig. S1a†), powerfully indicating that water gives rise to the development of porous structure. When further treated with a hydrothermal process, a chain of nanoparticles with single diameter of 50 nm is obtained, as shown in Fig. 2a. Meanwhile, the effect of hydrothermal time on the sample morphology is also investigated to determine the optimum nanostructure. The SEM images have been supplied in Fig. S2.† The morphologies of the sample obtained from 6 and 18 h hydrothermal process are indeed inhomogeneous, which suggests that hydrothermal time has a profound influence on the nanostructure. Nevertheless, the sample treated with 12 h hydrothermal treatment displays the nanosphere-shaped morphology. Furthermore, the

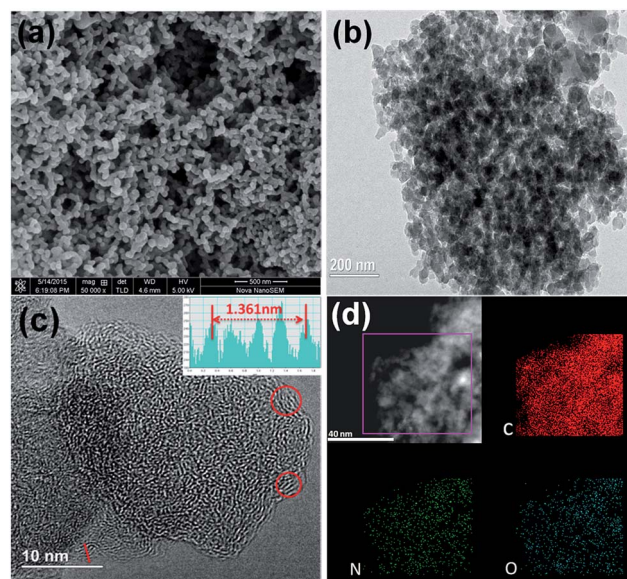


Fig. 2 (a) SEM images of hydrothermal product; (b) MCN-900 TEM image and (c) the corresponding high magnification TEM, the inset shows  $d$ -spacing of 5 stacking layers of graphene sheets; (d) STEM image of MCN-900 and EDS mapping of C, N, O.

morphology in Fig. 2b is kept as well as the appearance presented in Fig. 2a, even though the sample is subjected to high temperature treatment. Additionally, the HRTEM image of MCN-900 in Fig. 2c possesses a clear microporous and graphitized structure (marked by the red arrow), demonstrating the simple and efficient approach to producing porous carbon material through the hydrothermal method. In an attempt to further confirm the function of water, TEM and HRTEM images of the sample derived from carbonizing the original and absorbed water *Sterculia scaphigera* are also presented in Fig. S2.† Although both samples exhibit the irregular micromorphology in Fig. S1b and e,† the evident discrepancy in the porous and graphitized structure can be effortlessly distinguished. The consistent discrepancy is directly reflected from  $N_2$  adsorption/desorption and Raman characterization. These porous structures are believed to facilitate mass exchange during the ORR process and thereby improve the catalyst's performance.<sup>47</sup> The element mapping illustrated in Fig. 2d infers that carbon, nitrogen and oxygen are contained in the product and are dispersed homogeneously, indicating the successful doping of as-obtained carbon material.

Raman spectroscopy is a useful tool for revealing the electronic properties of carbon-based materials. The Raman spectra of Fig. 3 reveals that the D and G band were located around  $1360\text{ cm}^{-1}$  and  $1580\text{ cm}^{-1}$ , respectively. It can be seen that the G band arises from the bond stretching of all  $sp^2$ -bonds, including C–C, C–N and C–O, while the D band is associated with the  $sp^3$ -hybridized defect site.<sup>48</sup> In the Raman spectra of carbon-based materials, the parameter  $I_D/I_G$  is an interesting indicator of the level of defects within the material.<sup>9</sup> From Fig. 3, the  $I_D/I_G$  value is 1.23, 0.97 and 0.95 in the sequence of R-900 to MCN-900. Combined with the other results, it is confirmed that

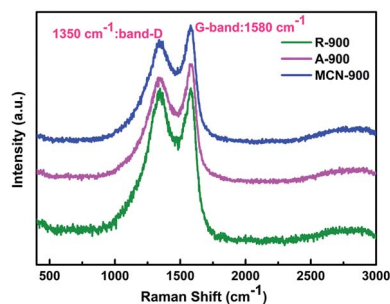


Fig. 3 Raman spectra for R-900, A-900 and MCN-900.

there is not only a defect caused by N doping, but there are also graphite-like planes with high temperature treatment (see Fig. S3†).

Surface area and pore distribution are important features of doped carbon materials in the context of their electrochemical activity. Fig. 4a and b show the nitrogen adsorption/desorption isotherms and pore size distribution of the three samples. A conspicuous feature of Fig. 4 is the different type of isotherms for these samples, as well as pore size distribution, which demonstrates the role of water in the preparation of porous carbon material. As shown in Fig. 4a, MCN-900 exhibits the typical type-IV isotherms, in sharp contrast to the type I isotherms of sample A-900 and R-900. In addition, the pore size distribution calculated using the BJH method is presented in Fig. 4b, indicating the hierarchical porous texture of MCN-900 and monotonous pore size of samples R-900 and A-900. The impact of water and temperature on the surface and pore size is listed in Table S1.† It can be seen from Table S1† that the BET specific surface area has been increased to  $353.87 \text{ m}^2 \text{ g}^{-1}$  for MCN-900, far more than that of R-900 at  $2 \text{ m}^2 \text{ g}^{-1}$ . Meanwhile, the pore size and volume of A-900 and MCN-900 have expanded enough to be identified from the data. These results are in accordance with the differences observed in the TEM image.

Fig. 5a displays a comparison of the XPS survey spectra obtained from R-900, A-900 and MCN-900 species, confirming the presence of C, N and O elements with N/C atomic ratios of 1.8%, 3.25% and 6.71%, respectively. The high resolution C 1s spectrum of sample MCN-900 (Fig. S4†) affirms the existence of effective function groups to improve ORR catalysis activity, such as C–N (285.2 eV) and C=O (288.3 eV). For insight into the amount and type of N-bonding configuration, the high-

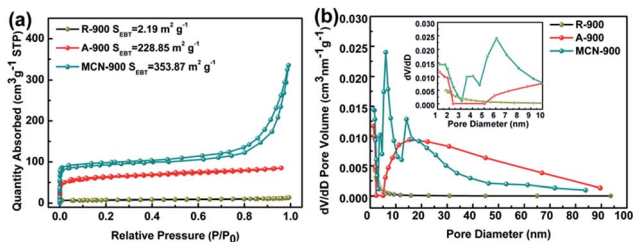


Fig. 4 (a) Nitrogen adsorption/desorption isotherms for R-900, A-900 and MCN-900; (b) pore size distribution of the corresponding species.

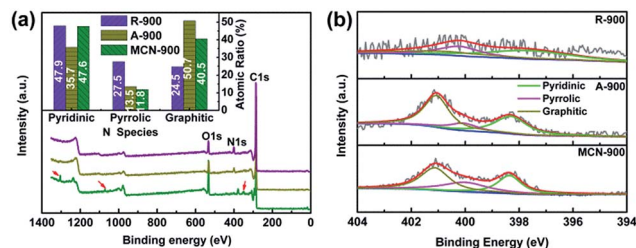
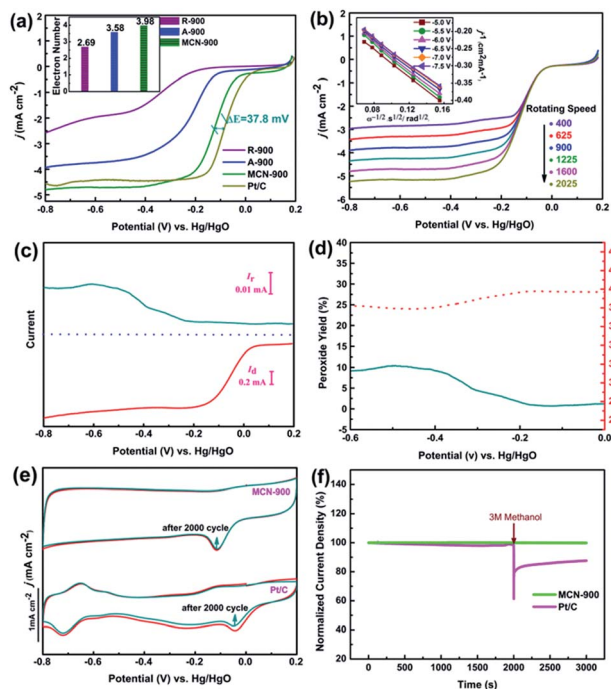


Fig. 5 (a) Full-scan XPS survey spectra of R-900, A-900 and MCN-900, the inset is atomic ratio of each N species for the corresponding sample; (b) high resolution N 1s XPS of R-900, A-900 and MCN-900.

resolution N 1s deconvolution analyses is shown in Fig. 5b. It can be seen in Fig. 5b that all of the samples contain three types of nitrogen configurations: pyridinic-N (398.9 eV), pyrrolic-N (399.8 eV), and quaternary N (401.2 eV). However an eye-catching difference is the amount of N species. Considering the inset of Fig. 5a and Table S2,† although a relatively high amount of pyridinic-N belongs to R-900, the total N content is merely 1.3 at%, far lower than in MCN-900. The N content will undoubtedly affect the electrochemical performance. It is supposed that this results from the consumption of impurities in raw material when annealing at high temperatures.<sup>49</sup> In Fig. 5a, there was still an observed impurity peak of R-900, shown by the red arrows. Based on these results, it can be reasonably speculated that the hydrothermal process contributes to retaining the N content and forms the efficient N species that promote electrochemical activity.<sup>50</sup>

### 3.2 Electrochemical activities

Inspired by the super chemical and physical properties of demonstrated by the MCN-900 sample, we expected that porous nanosphere-shaped carbon has great potential for application in ORR catalysis. The electrocatalytic performance for ORR was analyzed by rotating disk electrode (RDE) and rotating ring-disk electrode (RRDE) measurement in alkaline media (0.1 M KOH) and acidic media (0.1 M HClO<sub>4</sub>). A significant redox peak is found at approximately  $-0.11 \text{ V}$  for MCN-900 electrode in Fig. 5a and around  $-0.07 \text{ V}$  for Pt/C electrode in Fig. 6b, representing the reduction process in O<sub>2</sub>-saturated KOH solution.<sup>51,52</sup> In order to compare the electrocatalytic performance of all carbon materials in the ORR, linear sweep voltammetry (LSV) curves were performed on a rotating disk electrode in an O<sub>2</sub>-saturated 0.1 M KOH solution at a scan rate of  $10 \text{ mV s}^{-1}$  (Fig. 6c). The ORR performance is clearly enhanced as the preparation method changes. In particular, the sample MCN-900 obtained from the hydrothermal treatment shows more positive onset potential (around  $-0.02 \text{ V}$ ) than that of R-900 ( $-0.15 \text{ V}$ ) and A-900 ( $-0.095 \text{ V}$ ), which is on the verge of the onset potential 0.03 V of commercial Pt/C.<sup>7,53</sup> Moreover, the diffusion-limiting current density of the MCN-900 electrode reaches to  $-4.8 \text{ mA cm}^{-2}$ , superior to the Pt/C electrode at  $-4.6 \text{ mA cm}^{-2}$ . Considering that the electrocatalytic performance changes with different temperature treatments, the LSV curves of MCN-800 and MCN-1000 were also recorded at 1600 rpm, presented in Fig. S6.† Apparently the MCN-900 exhibits the



**Fig. 6** The ORR performance in 0.1 M KOH solution. (a) LSV curves of on R-900, A-900, MCN-900 and Pt/C at a rotation rate of 1600 rpm, the inset shows the corresponding electron transfer numbers; (b) LSV curves of the MCN-900 with various rotation rates at a scan rate of  $10 \text{ mV s}^{-1}$ , the inset is the corresponding Koutecky–Levich plots ( $j^{-1}$  vs.  $\omega^{-1/2}$ ) at different potentials; (c) RRDE voltammograms of MCN-900 in  $\text{O}_2$  saturated solution at rotation speed of 1600 rpm and sweep rate of  $10 \text{ mV s}^{-1}$ ; (d) the electron transfer and peroxide yields calculated from the RRDE measurement results; (e) electrochemical stability comparison of MCN-900 and commercial 20% Pt/C as determined by continuous CV scanning in  $\text{O}_2$ -saturated 0.1 M KOH solution, scan rate:  $10 \text{ mV s}^{-1}$ ; (f) current–time chronoamperometric responses of MCN-900 and commercial 20% Pt/C upon the introduction of 3 M methanol at  $-0.3 \text{ V}$ .

optimal ORR performance compared with what is mentioned above. The more positive onset potential, as well as the higher current density of MCN-900, may be attributed to the perfect synergistic effect of N species as well as the abundant porous structure, and enlarged specific surface area. Thus oxygen could be reacted onto the catalyst surface with the preferred configuration in a large quantity, and the electrons required for ORR could be readily transferred into the catalyst.

As is well known, electrocatalysts with rapid ORR kinetics and rich electron transfer to the adsorbed oxygen molecules are highly desired. Therefore, to further clarify the kinetics of carbon materials during the ORR process, their RDE curves were performed under various rotation rates and analyzed using the K–L equation, which is shown in Fig. 6b and S7.† The electrons transferred per  $\text{O}_2$  of R-900, A-900 and MCN-900 electrode were calculated to be 2.69, 3.58 and 3.98, respectively, suggesting the efficient one-step, 4-electron dominated ORR process of MCN-900 sample, as is the case for Pt/C catalyst.<sup>54,55</sup> Meanwhile, the RRDE measurements confirm the electron transfer number of approximately 4, as shown in Fig. 6d, and the amount of  $\text{H}_2\text{O}_2$  is less than 11%. Therefore the

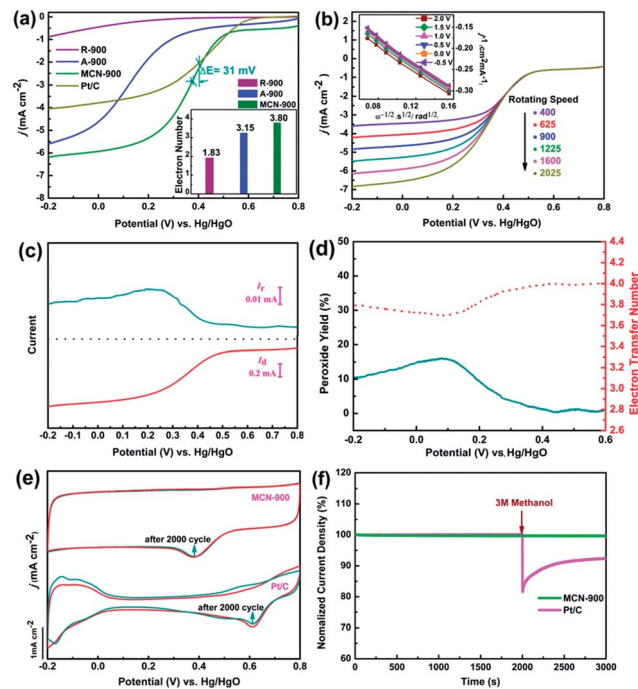


**Fig. 7** The ORR performance in 0.1 M  $\text{HClO}_4$  solution. (a) LSV curves of on R-900, A-900, MCN-900 and Pt/C at a rotation rate of 1600 rpm, the inset shows the corresponding electron transfer numbers; (b) LSV curves of the MCN-900 with various rotation rates at a scan rate of  $10 \text{ mV s}^{-1}$ , the inset is the corresponding Koutecky–Levich plots ( $j^{-1}$  vs.  $\omega^{-1/2}$ ) at different potentials; (c) RRDE voltammograms of MCN-900 in  $\text{O}_2$  saturated solution at rotation speed of 1600 rpm and sweep rate of  $10 \text{ mV s}^{-1}$ ; (d) the electron transfer and peroxide yields calculated from the RRDE measurement results; (e) electrochemical stability comparison of MCN-900 and commercial 20% Pt/C as determined by continuous CV scanning in  $\text{O}_2$ -saturated 0.1 M  $\text{HClO}_4$  solution, scan rate:  $10 \text{ mV s}^{-1}$ ; (f) current–time chronoamperometric responses of MCN-900 and commercial 20% Pt/C with the introduction of 3 M methanol at  $-0.3 \text{ V}$ .

method of using a four-electron pathway with high current to catalyze  $\text{O}_2$  reduction is feasible and efficient.

In view of practical applications in fuel cells, the MCN-900 electrode was therefore subjected to further testing with regards to the long-term stability and crossover effect for ORR. Fig. 6e shows the electrochemical stability plot for MNC-900 and 20% Pt/C catalysts. A noticeable reduction current with a well-defined cathodic peak (around  $-0.11 \text{ V}$ ) was maintained very well for MCN-900 electrode, whereas Pt/C shows an obvious diminution over the same period. This is possibly ascribed to the higher strength of the covalent C–N bond and the absence of activity degradation derived from Pt nanoparticle agglomeration and dissolution.<sup>56–58</sup> Fig. 6f illustrates the current–time chronoamperometric responses to 3 M methanol at the MCN-900 and Pt/C electrodes. There is no clear inversion of current density for MCN-900 after adding 3 M methanol, while a more distinct drop is observed for commercial Pt/C, implying the excellent tolerance of the MCN-900 electrode for methanol.

The ORR activity measurements in acidic media were carried out to further test this excellent catalytic performance. It is

obvious that a redox peak of MCN-900 with higher current density is observed from Fig. S8a† compared with Fig. S8b,† demonstrating an oxygen reduction process in acidic media. And even better catalytic activity is observed in Fig. 7a in comparison to that in alkaline media for MCN-900. The half-potential difference between MCN-900 and Pt/C is only at 31 mV. The ORR kinetics in acidic media is reflected in Fig. 7b, which shows good linearity in the inset. Through the K–L plot, it is calculated from linear fit lines that the number of electrons transferred is estimated to be 3.75–3.8 at the potential ranging from –0.05 to 0.2 V. A four-electron pathway for ORR accompanying high current is revealed in acidic media. RRDE measurements further confirm the ORR pathway, which is consistent with the result obtained from K–L analysis. Meanwhile, the low ring current of MCN-900 suggests that a low amount of hydro peroxide yields between 5–16% over a potential range of –0.2 to 0.6 V.

The long-term stability and tolerance to methanol poisoning effects in acidic media are also measured to reflect the potential for final applications, as shown in Fig. 6e and f. An almost negligible reduction current in the cathodic peak for MCN-900 is displayed in Fig. 7e, while Pt/C shows a dramatic current reduction after 2000 cycles. A more noticeable drop is found in Fig. 7f when 3 M methanol is introduced, whereas a small change is observed for MCN-900, demonstrating high methanol tolerance even in acidic media.

## 4 Conclusions

In this work, nitrogen doped porous carbon nanoparticles were successfully fabricated from *Sterculia scaphigera*, which is abundantly available and a constantly renewed natural source. With the assistance of water and hydrothermal treatment, it has been proven that not only pore texture and graphitization degree, but also the relative nitrogen content of three types of nitrogen species is significantly improved. The preparation approach is ordinary, but extremely successful and efficient, producing highly conductive porous carbon. In this case, these characteristics of carbon material show a perfect synergistic effect to enhance the electrocatalytic oxygen reduction activity for fuel-cell technologies. Further considering the effect of temperature on the structural and functional properties, the carbon material treated at 900 °C serves as an optimal ORR electrocatalyst with high selectivity, remarkable stability and excellent methanol tolerance in comparison to commercial 20% Pt/C electrodes in alkaline and acidic media. This kind of carbon material may be a promising alternative for costly Pt-based electrocatalysts in fuel cells. The preparation method validated in this study responds to the requirement to produce high quality and outstanding performance carbon-based electrocatalysts with a simple, cost-effective and environmentally benign approach.

## Acknowledgements

This work was supported by the National Natural Science Foundation of China (No. 21671096), Natural Science Foundation of Guangdong Province (No. 2016A030310376), the Natural

Science Foundation of Shenzhen (No. JCYJ20150630145302231, JCYJ20150331101823677), the Shenzhen Peacock Plan (KQCX20140522150815065). S. Y. thanks the support from the Guangdong and Shenzhen Innovative Research Team Program (No. 2011D052, KYPT20121228160843692).

## Notes and references

- 1 M. W. Kanan and D. G. Nocera, *Science*, 2008, **321**, 1072–1075.
- 2 J. Suntivich, K. J. May, H. A. Gasteiger, J. B. Goodenough and Y. Shao-Horn, *Science*, 2011, **334**, 1383–1385.
- 3 S. Wang, D. Yu and L. Dai, *J. Am. Chem. Soc.*, 2011, **133**, 5182–5185.
- 4 M. Winter and R. J. Brodd, *Chem. Rev.*, 2004, **104**, 4245–4270.
- 5 P. G. Bruce, L. J. Hardwick and K. Abraham, *MRS Bull.*, 2011, **36**, 506–512.
- 6 Y. Liang, Y. Li, H. Wang, J. Zhou, J. Wang, T. Regier and H. Dai, *Nat. Mater.*, 2011, **10**, 780–786.
- 7 S. Gao, K. Geng, H. Liu, X. Wei, M. Zhang, P. Wang and J. Wang, *Energy Environ. Sci.*, 2015, **8**, 221–229.
- 8 W. Niu, L. Li, X. Liu, N. Wang, J. Liu, W. Zhou, Z. Tang and S. Chen, *J. Am. Chem. Soc.*, 2015, **137**, 5555–5562.
- 9 Z. Ma, S. Dou, A. Shen, L. Tao, L. Dai and S. Wang, *Angew. Chem., Int. Ed.*, 2015, **54**, 1888–1892.
- 10 A. Morozan, B. Josselme and S. Palacin, *Energy Environ. Sci.*, 2011, **4**, 1238–1254.
- 11 W. Wang, R. Wang, S. Ji, H. Feng, H. Wang and Z. Lei, *J. Power Sources*, 2010, **195**, 3498–3503.
- 12 H. A. Gasteiger, S. S. Kocha, B. Sompalli and F. T. Wagner, *Appl. Catal., B*, 2005, **56**, 9–35.
- 13 H. Wang, R. Wang, H. Li, Q. Wang, J. Kang and Z. Lei, *Int. J. Hydrogen Energy*, 2011, **36**, 839–848.
- 14 Y. Bing, H. Liu, L. Zhang, D. Ghosh and J. Zhang, *Chem. Soc. Rev.*, 2010, **39**, 2184–2202.
- 15 G. Wu, K. L. More, C. M. Johnston and P. Zelenay, *Science*, 2011, **332**, 443–447.
- 16 Z.-S. Wu, S. Yang, Y. Sun, K. Parvez, X. Feng and K. Müllen, *J. Am. Chem. Soc.*, 2012, **134**, 9082–9085.
- 17 K. Parvez, S. Yang, Y. Hernandez, A. Winter, A. Turchanin, X. Feng and K. Müllen, *ACS Nano*, 2012, **6**, 9541–9550.
- 18 C. Shang, M. Li, Z. Wang, S. Wu and Z. Lu, *ChemElectroChem*, 2016, **3**, 1437–1445.
- 19 K. Gong, F. Du, Z. Xia, M. Durstock and L. Dai, *Science*, 2009, **323**, 760–764.
- 20 L. Yang, S. Jiang, Y. Zhao, L. Zhu, S. Chen, X. Wang, Q. Wu, J. Ma, Y. Ma and Z. Hu, *Angew. Chem., Int. Ed. Engl.*, 2011, **123**, 7270–7273.
- 21 Z. Yang, Z. Yao, G. Li, G. Fang, H. Nie, Z. Liu, X. Zhou, X. Chen and S. Huang, CrossRef, CAS, Web of Science® Times Cited, 37.
- 22 L. F. Chen, X. D. Zhang, H. W. Liang, M. Kong, Q. F. Guan, P. Chen, Z. Y. Wu and S. H. Yu, *ACS Nano*, 2012, **6**, 7092–7102.
- 23 I. Y. Jeon, S. Zhang, L. Zhang, H. J. Choi, J. M. Seo, Z. Xia, L. Dai and J. B. Baek, *Adv. Mater.*, 2013, **25**, 6138–6145.

- 24 I. Y. Jeon, H. J. Choi, S. M. Jung, J. M. Seo, M. J. Kim, L. Dai and J. B. Baek, *J. Am. Chem. Soc.*, 2012, **135**, 1386–1393.
- 25 Y. Zheng, Y. Jiao, J. Chen, J. Liu, J. Liang, A. Du, W. Zhang, Z. Zhu, S. C. Smith and M. Jaroniec, *J. Am. Chem. Soc.*, 2011, **133**, 20116–20119.
- 26 P. Chen, L.-K. Wang, G. Wang, M.-R. Gao, J. Ge, W.-J. Yuan, Y.-H. Shen, A.-J. Xie and S.-H. Yu, *Energy Environ. Sci.*, 2014, **7**, 4095–4103.
- 27 J. J. Zeng and Y. J. Lin, *Appl. Phys. Lett.*, 2014, **104**, 133506.
- 28 S. Wang, L. Zhang, Z. Xia, A. Roy, D. W. Chang, J. B. Baek and L. Dai, *Angew. Chem., Int. Ed.*, 2012, **51**, 4209–4212.
- 29 L. Qu, Y. Liu and J. B. Baek, *ACS Nano*, 2010, **4**, 1321–1326.
- 30 S. Wang, E. Iyyamperumal, A. Roy, Y. Xue, D. Yu and L. Dai, *Angew. Chem., Int. Ed. Engl.*, 2011, **123**, 11960–11964.
- 31 Q. Li, S. Zhang, L. Dai and L. S. Li, *J. Am. Chem. Soc.*, 2012, **134**, 18932–18935.
- 32 J. Liang, Y. Jiao, M. Jaroniec and S. Z. Qiao, *Angew. Chem., Int. Ed.*, 2012, **51**, 11496–11500.
- 33 Z. W. Liu, F. Peng, H. J. Wang, H. Yu, W. X. Zheng and J. Yang, *Angew. Chem., Int. Ed. Engl.*, 2011, **123**, 3315–3319.
- 34 C. H. Choi, M. W. Chung, H. C. Kwon, S. H. Park and S. I. Woo, *J. Mater. Chem. A*, 2013, **1**, 3694–3699.
- 35 Y. Zheng, Y. Jiao, L. Ge, M. Jaroniec and S. Z. Qiao, *Angew. Chem., Int. Ed. Engl.*, 2013, **125**, 3192–3198.
- 36 F. Braghiroli, V. Fierro, M. Izquierdo, J. Parmentier, A. Pizzi and A. Celzard, *Carbon*, 2012, **50**, 5411–5420.
- 37 J. S. Lee, G. S. Park, S. T. Kim, M. Liu and J. Cho, *Angew. Chem., Int. Ed. Engl.*, 2013, **125**, 1060–1064.
- 38 D. Zhao, J. L. Shui, L. R. Grabstanowicz, C. Chen, S. M. Commet, T. Xu, J. Lu and D. J. Liu, *Adv. Mater.*, 2014, **26**, 1093–1097.
- 39 G. Nam, J. Park, S. T. Kim, D. B. Shin, N. Park, Y. Kim, J. S. Lee and J. Cho, *Nano Lett.*, 2014, **14**, 1870–1876.
- 40 D. S. Su, *ChemSusChem*, 2009, **2**, 1009–1020.
- 41 C. Lavorato, A. Primo, R. Molinari and H. Garcia, *Chem.–Eur. J.*, 2014, **20**, 187–194.
- 42 E. Raymundo-Piñero, M. Cadek and F. Béguin, *Adv. Funct. Mater.*, 2009, **19**, 1032–1039.
- 43 W. Wang, Y. Wan, S. Wu, M. C. Li, L. Cao, F. Lv, M. Yang, S. Z. Fang, R. Sun and Z. Lu, *RSC Adv.*, 2015, **5**, 46558–46563.
- 44 N. S. Lewis and D. G. Nocera, *Proc. Natl. Acad. Sci. U. S. A.*, 2006, **103**, 15729–15735.
- 45 C. Wei, L. Yu, C. Cui, J. Lin, C. Wei, N. Mathews, F. Huo, T. Sritharan and Z. Xu, *Chem. Commun.*, 2014, **50**, 7885–7888.
- 46 Z. Y. Wu, P. Chen, Q. S. Wu, L. F. Yang, Z. Pan and Q. Wang, *Nano Energy*, 2014, **8**, 118–125.
- 47 C. You, X. Zen, X. Qiao, F. Liu, T. Shu, L. Du, J. Zeng and S. Liao, *Nanoscale*, 2015, **7**, 3780–3785.
- 48 X. Wang, J. Wang, D. Wang, S. Dou, Z. Ma, J. Wu, L. Tao, A. Shen, C. Ouyang and Q. Liu, *Chem. Commun.*, 2014, **50**, 4839–4842.
- 49 X. Jin, G. Zhang, Y. Hao, Z. Chang and X. Sun, *Chem. Commun.*, 2015, **51**, 15585–15587.
- 50 D. H. Guo, R. Shibuya, C. Akiba, S. Saji, T. Kondo and J. Nakamura, *Science*, 2016, **351**, 361–365.
- 51 C. Zhang, N. Mahmood, H. Yin, F. Liu and Y. Hou, *Adv. Mater.*, 2013, **25**, 4932–4937.
- 52 L. Wang, A. Ambrosi and M. Pumera, *Angew. Chem., Int. Ed.*, 2013, **52**, 13818–13821.
- 53 L. Chen, R. Du, J. Zhu, Y. Mao, C. Xue, N. Zhang, Y. Hou, J. Zhang and T. Yi, *Small*, 2015, **11**, 1423–1429.
- 54 S. Gao, H. Fan, X. Wei, L. Li, Y. Bando and D. Golberg, *Part. Part. Syst. Charact.*, 2013, **30**, 864–872.
- 55 M. S. El-Deab, T. Sotomura and T. Ohsaka, *Electrochem. Commun.*, 2005, **7**, 29–34.
- 56 H. Jin, H. Zhang, H. Zhong and J. Zhang, *Energy Environ. Sci.*, 2011, **4**, 3389–3394.
- 57 H. Zhong, H. Zhang, Z. Xu, Y. Tang and J. Mao, *ChemSusChem*, 2012, **5**, 1698–1702.
- 58 H. Zhong, H. Zhang, S. Liu, C. Deng and M. Wang, *ChemSusChem*, 2013, **6**, 807–812.